(Preprint) AAS 25-XXX

NAVIGATION DOPPLER LIDAR PERFORMANCE ASSESSMENT AND TRAJECTORY RECONSTRUCTION OF THE INTUITIVE MACHINES IM-1 LUNAR LANDING

Christopher D. Karlgaard[*], Rafael A. Lugo[†], Jeremy D. Shidner[‡], Glenn D. Hines[§], Farzin Amzajerdian[¶], Aram Gragossian[‖], Daniel K. Litton[**] and Scott R. Angster[††]

The Navigation Doppler Lidar instrument was developed at NASA Langley Research Center to support precision landing at locations such as the Moon and Mars. The instrument uses a frequency modulated continuous wave method that provides simultaneous range and velocity measurement data that can be processed in an onboard navigation filter for vehicle state estimation. The sensor has been tested thoroughly in laboratory settings and on various helicopter and suborbital rocket flight tests. The Navigation Doppler Lidar instrument was recently flown as a payload onboard the Intuitive Machines mission IM-1, which was designed to soft-land on the surface of the Moon on February 22nd, 2024. The instrument provided valid measurements at ranges that exceeded preflight expectations. This paper describes the post-flight data processing and trajectory reconstruction of the IM-1 lander based on data from the Navigation Doppler Lidar and an onboard Inertial Measurement Unit. A Kalman filter was used to combine the data sources to reconstruct the approximate final three minutes of the trajectory prior to touchdown, where both sets of data were available. A digital elevation map was used to model the lunar surface terrain in the Kalman filter, and a ray tracing terrain engine was used to model the lidar beams. The results of the reconstruction show agreement between the lidar and modeled measurements to within approximately 5 m and 0.5 m/s, indicating that the Navigation Doppler Lidar provided accurate measurements and providing additional flight validation of the ray tracing terrain engine and underlying digital elevation map.

INTRODUCTION

NASA Langley Research Center's (LaRC) Navigation Doppler Lidar (NDL) instrument was developed to provide an onboard sensing solution for landing vehicles to meet the requirements of safe and precise landings on planetary bodies.[1] The NDL provides line-of-sight range and velocity measurements that can be used to aid the on-board Guidance, Navigation, and Control (GN&C) systems. Prior landers have made use of radar measurements to provide updates to the navigation state of the vehicle used in the on-board closed-loop GN&C.[2–4]

NDL sensors have recently reached the maturity to be considered as replacement sensors, due to a combination of ground testing and flight testing. The Autonomous Landing and Hazard Avoidance Technology (ALHAT) project[5] conducted a series of helicopter flight test campaigns in August 2008 at NASA Dryden (now Armstrong) Flight Research Center,[6,7] and December 2012 at NASA Kennedy Space Center (KSC).[8] These flight tests successfully demonstrated real-time NDL sensing

[*]Aerospace Engineer, Analytical Mechanics Associates, Inc., Hampton, VA. Member AAS, Associate Fellow AIAA.
[†]Aerospace Engineer, Atmospheric Flight and Entry Systems Branch, NASA Langley Research Center, Hampton, VA.
[‡]Aerospace Engineer, Atmospheric Flight and Entry Systems Branch, NASA Langley Research Center, Hampton, VA. Associate Fellow AIAA.
[§]Electrical Engineer, Engineering Integration Branch, NASA Langley Research Center, Hampton, VA.
[¶]Electrical Engineer, Remote Sensing Branch, NASA Langley Research Center, Hampton, VA.
[‖]Electrical Engineer, Remote Sensing Branch, NASA Langley Research Center, Hampton, VA.
[**]Project Manager, Space Technology and Exploration Directorate, NASA Langley Research Center, Hampton, VA.
[††]Service Delivery Manager, Analytical Mechanics Associates, Inc., Hampton, VA.

capabilities and the performance of the altitude and velocity estimates in comparison with integrated Global Positioning System (GPS) and Inertial Measurement Unit (IMU) navigation solutions. The ALHAT project conducted six flight tests of the NDL sensor on the rocket powered Morpheus test vehicle at KSC in 2014.[9,10] The first three flights with the NDL were open-loop (meaning the sensor was collecting data but not used in the on-board GN&C) for assessing sensor performance, and the last three tests used the sensors in the closed-loop GN&C for demonstration of the ALHAT navigation system. The open-loop flight tests showed that the NDL velocities agreed with the Morpheus navigation state to within 5 cm/s.[11] These flight tests successfully demonstrated the real-time closed-loop performance of a navigation filter that ingested NDL velocity measurements for precision landing.

Suborbital rocket-based flight testing of the NDL was carried out under the CoOperative Blending of Autonomous Landing Technology (COBALT) project, which flew several tethered and free flight tests onboard the Masten Space Systems (MSS) Xodiac suborbital rocket in 2017, in Mojave, CA.[12,13] The NDL sensor was flown in an open-loop data collection mode for post-flight performance evaluation, while the Xodiac test vehicle used its own GPS-aided inertial navigation for closed-loop GN&C.[12] These flight tests completed all objectives and demonstrated the real-time navigation filter that ingested NDL velocity and range measurements. The experimental navigation filter based on the COBALT sensors agreed with the Xodiac GPS/IMU navigation solution to within approximately 5 m in position and 0.5 m/s in velocity.

Further flight testing of the NDL was conducted during the Safe and Precise Landing - Integrated Capability Evolution (SPLICE) project,[14] which supported rocket sled tests at the Naval Air Weapons Station China Lake.[15] These tests were designed to stress the upper limits of NDL velocity and range measurements. The tests demonstrated the ability of the NDL to track the target at velocities above 200 m/s and at ranges up to 4 km. The SPLICE project flew NDL sensors on the Blue Origin New Shepard suborbital rocket on two flights in 2020 and 2021.[16] The NDL operation was adversely affected by the helium environment of the New Shepard rocket during these flights and provided limited measurements. Attempts for mitigating the effect of the rocket environment before the second flight was not successful and the NDL performance could not be evaluated.[17]

The NDL sensor has been considered for closed-loop GN&C and its impact on trajectory performance for precision landing of human-scale landing systems in simulation studies. These studies included linear covariance[18] and Monte Carlo 6 Degree-Of-Freedom (DOF) trajectory analysis[19,20] techniques at landing sites on the Moon and Mars. The findings in Reference 19 indicate that the use of NDL on a human-scale Mars entry system can significantly improve the both the likelihood of safe landing, and precision of the landing in a Monte Carlo statistical sense.

Recently, a NDL sensor was flown as a payload on the Intuitive Machines (IM) IM-1 lunar lander.[21] IM was selected by the NASA Commercial Lunar Payload Services (CLPS) program for providing delivery of payloads to the lunar surface. The first such mission, IM-1, flew a variety of NASA, educational, and commercial payloads, including a NDL, to the Moon in February, 2024.[22] The NDL sensor flown on IM-1 was intended to be used as a secondary navigation sensor during the mission, but software issues prevented the navigation filter from ingesting the data. In this work, the NDL data acquired during the IM-1 lunar landing were combined with linear accelerations and angular rates recorded by an IMU in a Kalman filter to reconstruct the descent and landing trajectory of the vehicle for post-flight analysis and performance assessment of the sensor. This process also permitted the evaluation and validation of the models used to simulate terrain and NDL beam data in the filter.

INTUITIVE MACHINES IM-1 MISSION OVERVIEW

The Intuituve Machines IM-1 mission to the lunar surface was launched from KSC on a SpaceX Falcon 9 launch vehicle on 06:05:00 February 15th, 2024, UTC, carrying the Nova-C class lander named *Odysseus*.[22] The vehicle was 3.9 m tall by 1.6 m in diameter with a hexagonal cross section, with a wet mass at launch of 2035 kg and dry mass of 677 kg.[22] A diagram of the lander is shown in

Figure 1.[22] The spacecraft performed three trajectory correction maneuvers during transit, followed by a lunar orbit insertion maneuver that placed the spacecraft in a 20 by 200 km altitude orbit on February Feb 21st, 2024, 14:35:51 UTC.[22,23]

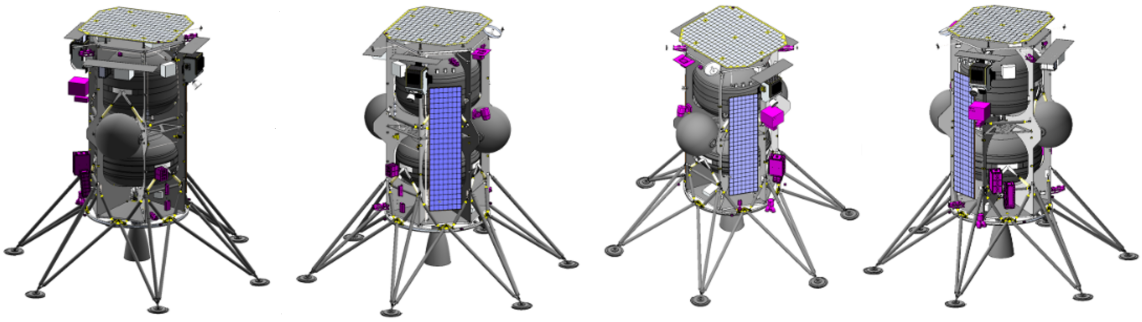

Figure 1. IM-1 Odysseus lander.[22]

The Odysseus lander's GN&C system included an array of sensors including an IMU, optical feature tracking for terrain-relative navigation, and a laser altimeter to provide autonomous navigation solutions from a Kalman filter that was initialized based on orbit determination from the Deep Space Network (DSN).[24,25] The NDL velocity measurements were intended to be used as secondary inputs to the navigation filter.[21] The outputs of the filter provided the navigation state to the vehicle guidance and control during its descent and landing on the lunar surface.

A discovery was made prior to descent initiation that the laser altimeter was not operational and could not provide data to the navigation filter. Thus, the filter would rely on IMU and optical feature tracking alone. An effort was made to modify the flight software to enable processing of the NDL range and velocity measurements, however the attempt proved to be unsuccessful and the vehicle conducted its landing without the use any NDL data.[21,24]

The de-orbit insertion maneuver was executed on Feb 22, 20214 at 05:49:29 UTC[23] followed by initiation of the powered lunar landing sequence on February Feb 22nd, 2024, 23:10:32 UTC.[22] Odysseus landed near the Malapert-A crater at the location -80.1276 deg N, 1.4367 deg E on February 22nd, 2024 at 23:23:00 UTC.[24] Details of the powered flight post-flight performance reconstruction can be found in Reference 24.

DATA SOURCES

The data sources available for producing the reconstruction include an IMU in addition to the NDL sensor data. Terrain and gravitational model data were also used in conjunction with the NDL and IMU sensor data, respectively.

Coordinate frames required for the data processing and reconstruction analysis are described as follows. The Nova-C vehicle body frame is denoted as the $\mathcal{N}$ frame. The origin of the frame is in the plane formed by the vehicle landing pads, and the positive x-axis of this frame is along the centerline of the vehicle away from the ground when landed.[23] The NDL sensor frame is denoted by $\mathcal{S}$ and is fixed in the Nova-C body frame as shown in Figure 4.

The topocentric, $\mathcal{C}$, frame is a body-carried frame in which the z-axis is oriented toward the center of the moon, the y-axis is to the east, and the x-axis is oriented towards geographic North and completes the right-handed system.[26] The topodetic, $\mathcal{D}$, frame is similar to the topocentric frame but has its z-axis oriented downwards perpendicular to the lunar reference ellipse and x-axis tangent to the reference ellipse to the north.[26] The $\mathcal{M}$ frame is a Moon-Centered Moon-Fixed frame where the xy plane corresponds to the Moon's mean equator and the z-axis is perpendicular to the mean equator torwards the north pole.

Navigation Doppler Lidar

The NDL instrument uses a frequency modulated continuous wave (FMCW) approach to measure line of sight (LOS) ranges and velocities from three laser beams fixed at different pointing angles in the instrument. The NDL was designed to measure velocities up to $\pm$ 218 m/s along the LOS of its beams and ranges from 5 km to 2 m,[27] at a sample rate of 20 Hz. Testing and calibration of the instrument indicated 1σ range and velocity measurement uncertainties of $\left(1.2 \cdot 10^{-4}\rho + 0.16\right)$ m and $\left(1.11 \cdot 10^{-6}\rho + 1.4 \cdot 10^{-3}\right)$ m/s, respectively.

The instrument consists of an electro-optic chassis and an optical head. All of the lidar components including the transmitter laser, receivers, and signal processor are housed in the electro-optic chassis. The optical head, housing three transmit/receive lenses, is mounted rigidly on the vehicle with a clear field-of-view to the ground, and connected to the electro-optic chassis through a fiber optic cable carrying the transmitted beams to the lenses and directing the returned signals collected by the same lenses to the receivers. The full transmit to received signal processing chain for each beam is called a *channel*. The NDL electro-optic chassis and optical head are shown as installed on the IM-1 Odysseus lander in Figure 2.

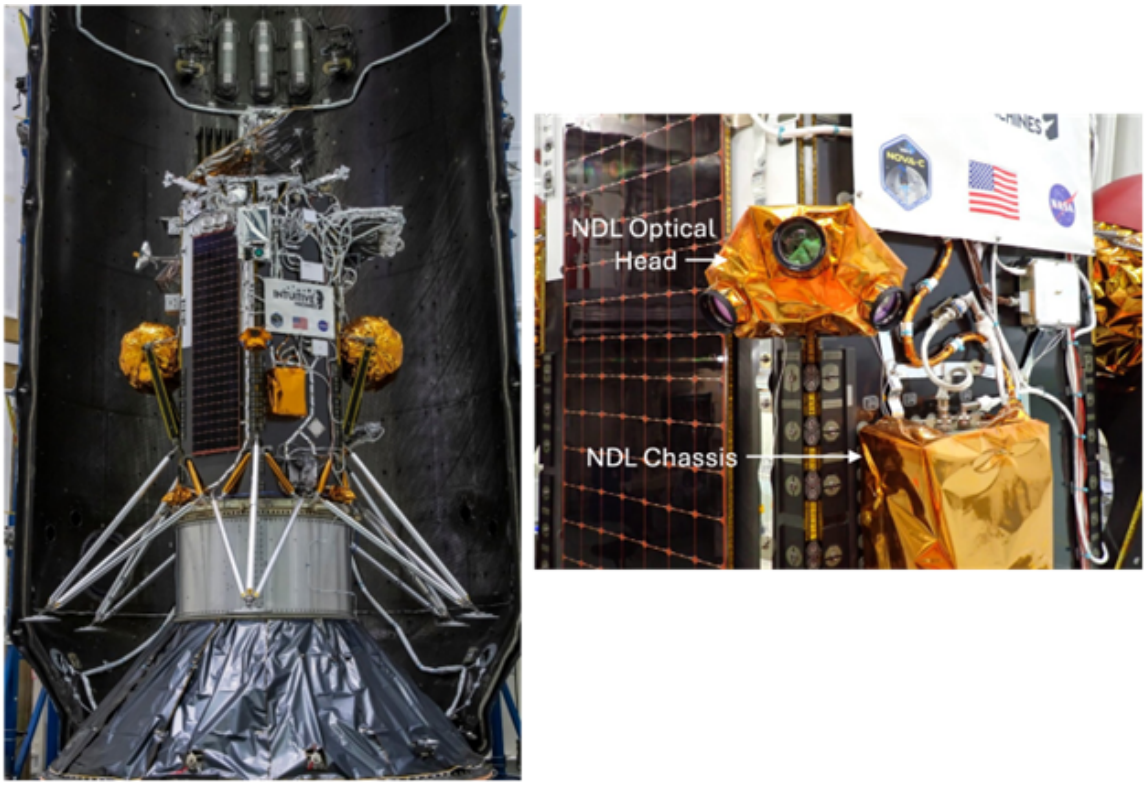

Figure 2. NDL installed on IM-1 Odysseus lander.

The nominal NDL sensor beam pointing directions are illustrated in Figure 3. Beam A was oriented at an 80 deg angle relative to the vehicle centerline. Beams B and C were symmetric with an angle of 57.5 deg relative to the centerline and $\pm$ 42.5 deg outboard. The NDL sensor coordinate frame is shown in Figure 4. These pointing directions were chosen to capture long range measurements based on the expected vehicle trajectory and orientation. The channel A telescope was designed to be pointed close to nadir during most of the vehicle's descent.

The as-installed beam pointing directions expressed in the NDL sensor frame $\mathcal{S}$ are

$$\boldsymbol{S} = \begin{bmatrix} \boldsymbol{s}_A^{\mathsf{T}} \\ \boldsymbol{s}_B^{\mathsf{T}} \\ \boldsymbol{s}_C^{\mathsf{T}} \end{bmatrix} = \begin{bmatrix} 0.98430 & -0.00241 & 0.17647 \\ 0.61990 & -0.56916 & 0.54017 \\ 0.61986 & 0.56790 & 0.54106 \end{bmatrix} \tag{1}$$

Post-installation metrology indicated a 1 mrad uncertainty in the beam installation directions. This error source was applied as a 1σ uncertainty independently to both the beam alignment within the NDL frame, and to the NDL sensor frame alignment to the Nova-C vehicle body frame.

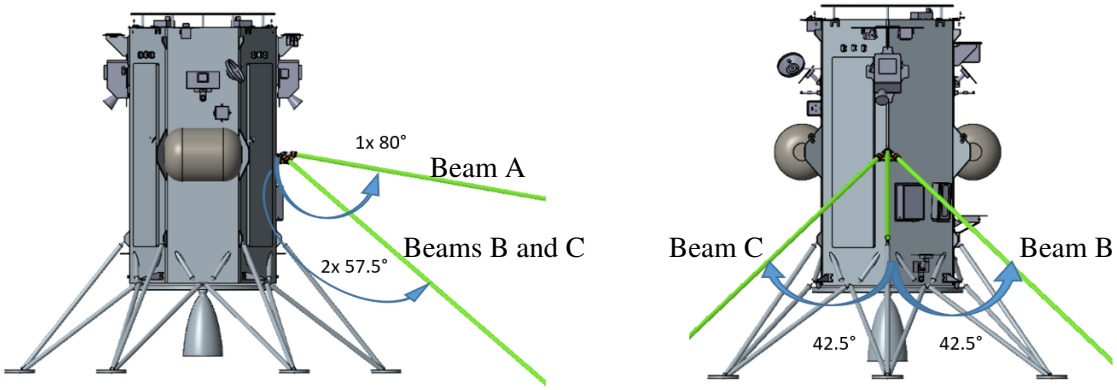

Figure 3. NDL installation in the IM-1 lunar lander.

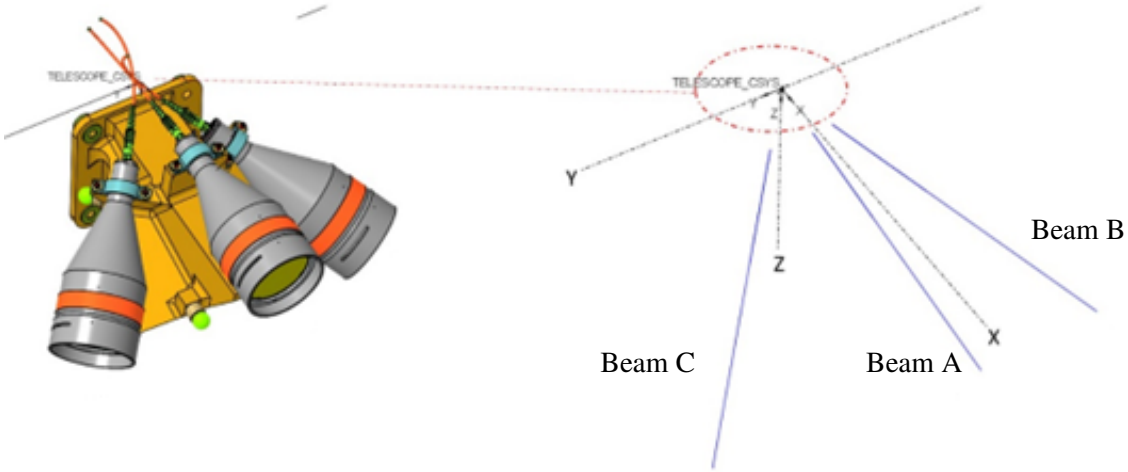

Figure 4. NDL sensor frame.

The transformation from the NDL sensor frame to the Nova-C vehicle body frame is

$$\boldsymbol{R}_{\mathcal{SN}} = \begin{bmatrix} 0 & 0 & -1 \\ 0 & 1 & 0 \\ 1 & 0 & 0 \end{bmatrix} \tag{2}$$

The as-installed NDL sensor origin point O relative to the Nova-C vehicle body frame origin is

$$\boldsymbol{r}_{NO} = \begin{bmatrix} 1.402 & -0.055 & 0.844 \end{bmatrix}^{\mathsf{T}} \text{m} \tag{3}$$

The notional orientation of the beams relative to the lunar surface are illustrated in Figure 5. Here, the vehicle is moving from left to right as it decelerates towards the designated landing site. Beam A in the center is oriented towards the nadir direction slightly in trail. Beams B and C are oriented further outward and down toward the landing legs such that the beams are directed ahead of the vehicle as it descends to the surface.

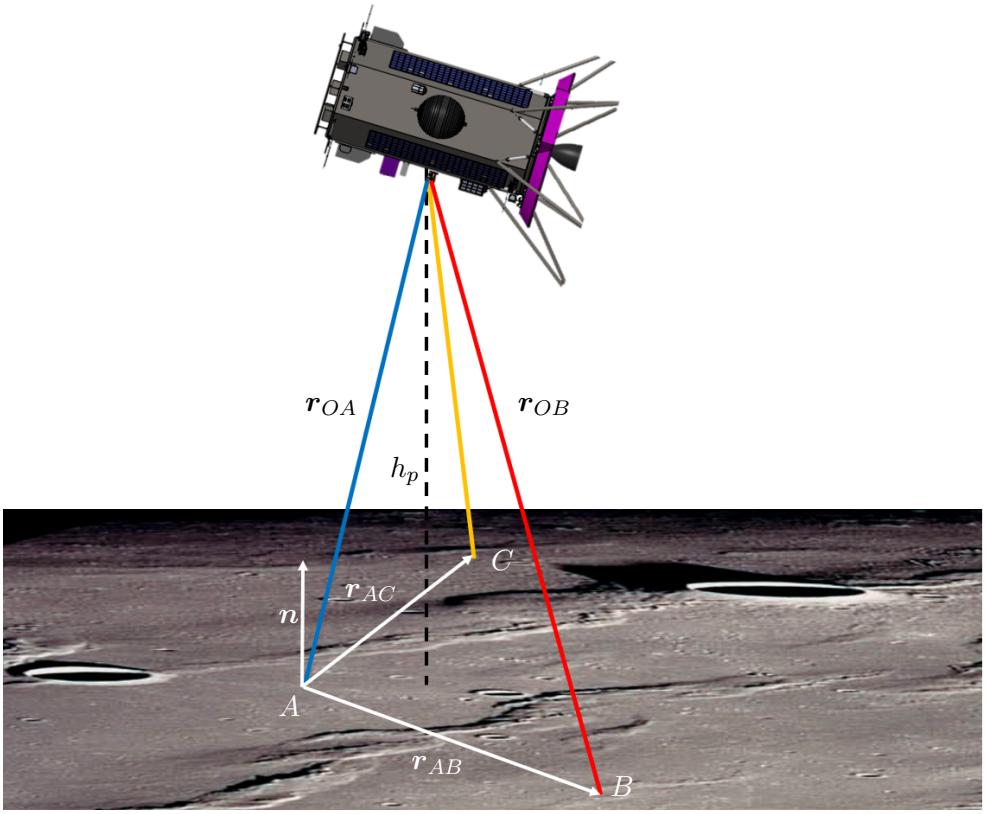

Figure 5. NDL beam/surface intersection geometry.

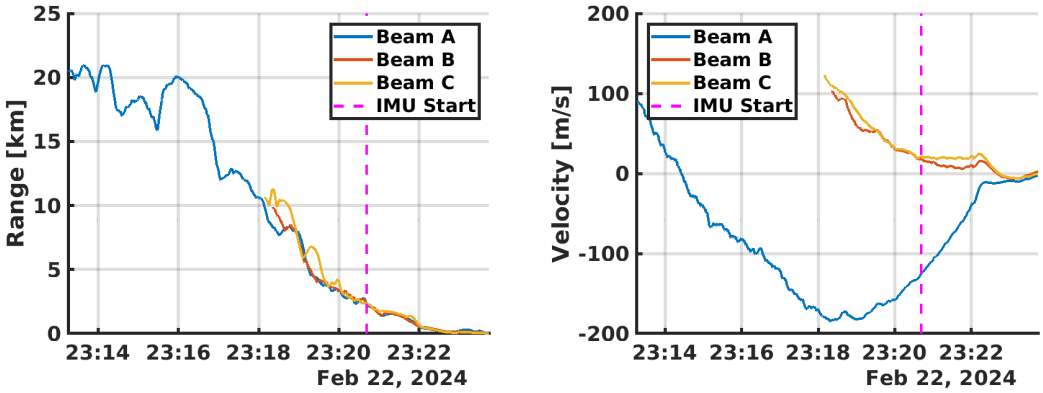

(a) Beam ranges.

(b) Beam velocities.

Figure 6. NDL ranges and velocities.

The NDL range and velocity measurements obtained during the IM-1 lunar landing are shown in Figure 6. Beam A, pointing nearly nadir, was able to measure ranges of more than 20 km, in excess of the expected 5 km performance. Beams B and C reported ranges of more than 10 km after 23:18 UTC during descent. All three beams intersect with the lunar surface and provide range and velocity data from 23:18:20.6 UTC in time until touchdown at 23:23:45.0 with no dropouts or outliers. The total duration of the data set included approximately 629 s of Beam A range and velocity measurements, 324 s of Beam B, and 336 s of Beam C. Note that the final data point shown in Figure 6 corresponds to the vehicle's first contact with the lunar surface.

The start of the provided IMU data set at 23:20:41.34 UTC is indicated in Figure 6 by the vertical

dashed black line. The complete 6-DOF trajectory reconstruction is limited to this segment of the landing, though some trajectory information can be obtained from the NDL measurements alone earlier in the trajectory as will be discussed later in the paper. The IMU data are discussed further in the next section.

There are several noteworthy features in the measured data. The channel A range measurement shows an increase/decrease feature that peaks at approximately 23:16 UTC. The channel C range measurement shows a deviation from the channel A and B measurements at 23:18:40 UTC. Three smaller deviations can be noted in channel C starting at approximately 23:19:20, 23:19:57, and 23:21:47 UTC. These deviations were likely due to the beam intersecting several craters during descent. Note that the corresponding velocity channels do not show any sizable deviations during these crater intersections. The insensitivity of the NDL velocity measurements to crater impingement is because the NDL velocities are produced independently from range. Also note that channel A has negative velocity measurements over the majority of the trajectory while channels B and C have positive measurements. This is because of the position and pointing of the optical head, where channel A has a view of the ground where the terrain is receding from the vehicle, while B and C have a view where the terrain is approaching the vehicle, as indicated in Figure 5.

Inertial Measurement Units

The IM-1 lunar lander had two IMUs that were recording data during the landing. The IMUs provided linear acceleration and angular rate data in the spacecraft body frame. The first IMU was a Honeywell HG1700 with a sample rate of 100 Hz and the second IMU was an Emcore SDI-505 with a sample rate of 200 Hz. The data were compared and found to be in agreement. The IMU data were limited to approximately the last 184 s of the trajectory due to constraints on the data volume that could be sent back to Earth for post-flight analysis. The 200 Hz sample rate Emcore SDI-505 IMU was chosen as the primary sensor for purposes of this trajectory reconstruction due to its higher sample rate. Other performance specifications of the two IMU models are generally comparable as shown in Table 1, based on publicly available vendor specification sheets. Note that internal misalignment specifications were not available for either unit and were assumed to be negligible. No further details are shown here due to the proprietary nature of the data.

Table 1. IMU performance specifications.

Parameter	HG1700	SDI-505
Accelerometer Bias, mg (3σ)	3	3
Accelerometer Scale Factor, ppm (3σ)	900	600
Accelerometer Random Walk, m/s/$\sqrt{\text{hr}}$ (3σ)	0.02	0.177
Gyroscope Bias, deg/hr (3σ)	3	3
Gyroscope Scale Factor, ppm (3σ)	450	600
Gyroscope Random Walk, deg/$\sqrt{\text{hr}}$ (3σ)	0.125	0.02
Sample Rate, Hz	100	200

Terrain Models

Accurate modeling and simulation of the lunar surface is a key component to pre- and post-flight analysis of spacecraft performance. Digital Elevation Models (DEMs) are often used for these applications and typically contain surface elevation data measured from a reference sphere at gridded coordinates. In this work, a DEM representing a region of the lunar south pole below 75 deg south latitude at a resolution of 30 m per pixel using polar-stereographic coordinates is used, and a similar DEM of 20 m per pixel resolution was used below 80 deg south latitude.[28] Data from the 30 m per pixel DEM is shown in Figure 7 corresponding to the region from 75 deg south latitude to the south pole. These DEMs are the best resolution sets of data currently available from the Lunar Orbiter Laser Altimeter (LOLA) science team[28] in the region of interest for the IM-1 NDL

data analysis. In this work, the DEM representation of the surface was assumed to be truth and no uncertainty was applied to the elevations.

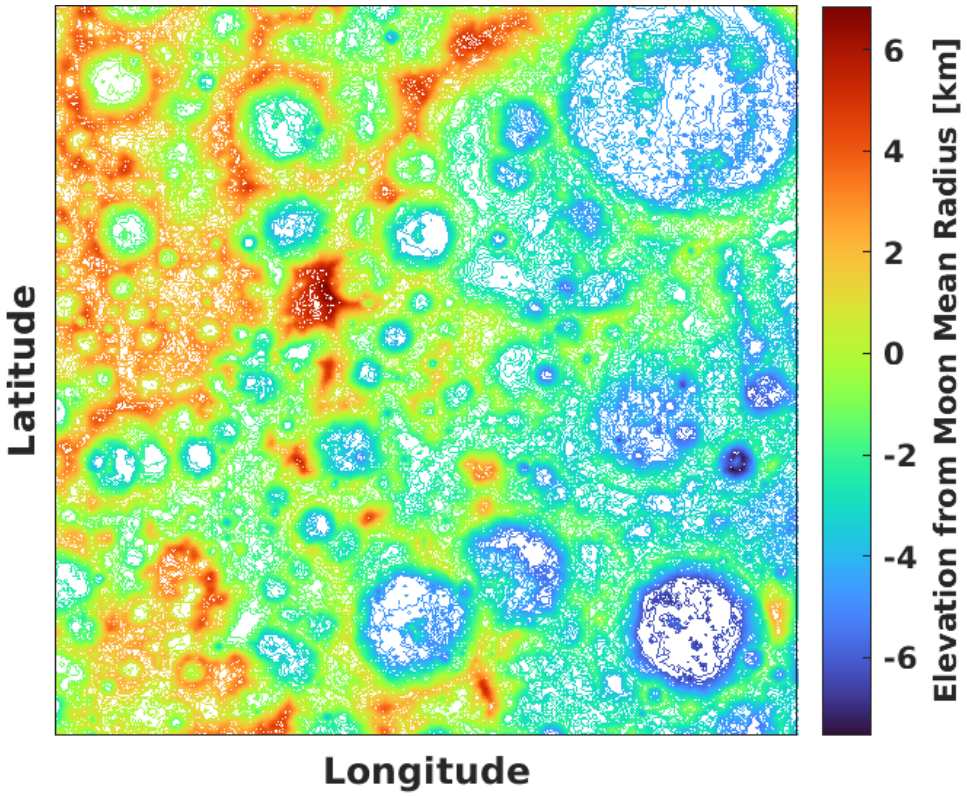

Figure 7. Lunar DEM: 75 to 90 deg south latitude, with 30 m per pixel resolution.

Gravity Model

The gravitational accelerations used for integrating the equations of motion were based on a model developed from data acquired during the Gravity Recovery and Interior Laboratory (GRAIL)[29] spacecraft pair experiment. Inter-spacecraft range measurements and other tracking data from the primary GRAIL science mission were used to construct the 660 degree and order gravitational model GRGM660PRIM.[29] In this work, a truncated 25 degree and order set of spherical harmonics from the GRGM660PRIM model were used to computing the graviational accelerations for the trajectory reconstruction process.

Post-Mission Trajectory

Intuitive Machines provided a post-mission trajectory that was constructed using the Copernicus trajectory optimziation software.[30] The software was configured to fit certain known observables and navigation states during the descent and landing to the lunar surface. This trajectory was used to analyze NDL performance prior to the start of the IMU data. This trajectory was also used to provide the initial conditions for the Kalman filter-based trajectory reconstruction described in this paper. Further details on the development of this trajectory can be found in Reference 24.

TRAJECTORY RECONSTRUCTION METHODS

This section describes the methods used for the NDL/IM-1 trajectory reconstruction. These include a geometric approach for processing the three NDL beam range and velocity measurements to reconstruct some limited trajectory data during the descent and landing, and a Kalman filter method that processes the NDL measurements with the IMU to estimate the 6-DOF vehicle trajectory.

NDL-Only Analysis

The Kalman filter approach described in the previous section is restricted to the last three minutes of the trajectory due to the limited amount of IMU data that was returned. Some trajectory information can be obtained by analyzing the NDL beam ranges and velocities during the two minutes of twenty seconds of time prior to the start of the IMU data, where all three beams intersect with the lunar surface after 23:18:20.6 UTC as shown Figure 6.

The body-axis velocity vector can be computed directly from the beam velocities and the NDL sensor pointing matrix as,

$$\boldsymbol{V} = \left\{ \begin{array}{c} V_x \\ V_y \\ V_z \end{array} \right\} = \boldsymbol{R}_{\mathcal{SN}} \boldsymbol{S}^{-1} \left\{ \begin{array}{c} \nu_A \\ \nu_B \\ \nu_C \end{array} \right\} \tag{4}$$

The beam velocity angles can be computed from the reconstructed body-axis velocity and the pointing directions as

$$\eta_A = \cos^{-1}\left(\boldsymbol{V} \cdot \boldsymbol{R}_{\mathcal{SN}} \boldsymbol{u}_A / \|\boldsymbol{V}\|\right) \tag{5}$$

with similar expressions for Beams B and C. The angles of attack and sideslip can be computed from the body-axis velocity as

$$\beta = \sin^{-1}\left(\frac{V_y}{\|\boldsymbol{V}\|}\right) \tag{6}$$

$$\sin\alpha = \frac{V_z}{\|\boldsymbol{V}\| cos\beta} \tag{7}$$

$$\cos\alpha = \frac{V_x}{\|\boldsymbol{V}\| cos\beta} \tag{8}$$

$$\alpha_T = \cos^{-1}\left(\cos\alpha \cos\beta\right) \tag{9}$$

An estimate of the altitude can be computed from the three simultaneous range measurements. The range measurements from the NDL origin (point O) to the surface form the vertices of a triangle at points A, B, and C that form the plane containing the beam/surface intersection points. The edges of the triangle are formed by the vectors $\boldsymbol{r}_{AB} = \boldsymbol{r}_{OB} - \boldsymbol{r}_{OA}$, $\boldsymbol{r}_{AC} = \boldsymbol{r}_{OC} - \boldsymbol{r}_{OA}$, and $\boldsymbol{r}_{BC} = \boldsymbol{r}_{OC} - \boldsymbol{r}_{OB}$, where $\boldsymbol{r}_{OA} = \rho_A \boldsymbol{s}_A$, $\boldsymbol{r}_{OB} = \rho_B \boldsymbol{s}_B$, and $\boldsymbol{r}_{OC} = \rho_C \boldsymbol{s}_C$. The geometry of the vector measurements are illustrated in Figure 5.

The surface normal that defines the plane containing the intersection points can be computed from the cross product[1]

$$\boldsymbol{n} = \frac{\boldsymbol{r}_{AB} \times \boldsymbol{r}_{AC}}{\|\boldsymbol{r}_{AB} \times \boldsymbol{r}_{AC}\|} \tag{10}$$

The height of the NDL origin relative to this plane can then be computed from the projection of any one range measurement along the surface normal, such as

$$h_p = -\boldsymbol{r}_{OA} \cdot \boldsymbol{n} \tag{11}$$

The beam incidence angle, pitch angle, and flight path with respect to the lunar surface normal can be computed from the equations

$$\lambda_A = \cos^{-1}\left(-\boldsymbol{s}_A \cdot \boldsymbol{n}\right) \tag{12}$$

$$\zeta = \pi/2 - \cos^{-1}\left(\left[\begin{array}{ccc} 0 & 0 & -1 \end{array}\right]^{\mathsf{T}} \cdot \boldsymbol{n}\right) \tag{13}$$

$$\gamma = \pi/2 - \cos^{-1}\left(\boldsymbol{R}_{\mathcal{SN}}^{\mathsf{T}} \boldsymbol{V} \cdot \boldsymbol{n} / \|\boldsymbol{V}\|\right) \tag{14}$$

In summary, the body-axis velocities, velocity angles, incidence angles, height above the beam-surface intercept plane, the pitch angle, and flight path angle relative to the plane can be estimated. Thus, some trajectory information can be obtained based solely on the NDL measurement data where all three beams have returned valid measurements.

New Statistical Trajectory Estimation Program

The New Statistical Trajectory Estimation Program (NewSTEP) is a Matlab-based iterative extended Kalman filter/smoother code that has been formulated specifically for solving post-flight trajectory reconstruction problems.[26,31] The code has been used on numerous other trajectory reconstruction problems over the last two decades. Notably, the Mars Science Laboratory[32] and Mars 2020[33] missions both flew a radar Terminal Descent Sensor (TDS)[4] that provided slant range and velocity data of a similar form to that of the NDL, thus providing prior validation of the measurement models used in the filter.

The code functions as a forward and backward filtering passes through the measurement data that are combined using a Fraser-Potter smoother. The filter states are expressed in spherical coordinates relative to the center of the primary body. The equations of motion are propagated from one measurement point to another by numerical integration of the IMU measured linear accelerations and angular rates. The filter was configured for this problem to "consider" all IMU measurement systematic errors and the NDL beam alignment uncertainties for realistic covariance estimates. The code outputs position, velocity, and attitude in various coordinate systems, and from those outputs, other quantities of interest for this problem can be calculated including the beam incidence angles and other outputs described in the previous subsection. Note that the incidence angles and other surface-relative quantities are calculated from the DEM surface normal rather than the beam/surface intersection plane formed by the three range measurements as in the previous section.

Filter Process Model The filter state for this problem is specified as the position, velocity, and attitude of the vehicle with respect to the center of the moon, expressed in a rotating coordinate frame fixed to the vehicle. The state of the system is

$$\boldsymbol{x} = \begin{bmatrix} r & \phi & \theta & u & v & w & e_0 & e_1 & e_2 & e_3 \end{bmatrix}^{\mathsf{T}} \tag{15}$$

where r, ϕ, and θ are the radius, declination, and longitude of the vehicle with respect to the moon center, u, v, and w are the inertial velocity components expressed in the topocentric frame where w is along the radial direction, v is to the east, and u is towards the north, and e_0, e_1, e_2, and e_3 are the Euler parameters that describe the attitude of the vehicle with respect to a local topodetic frame.

The process model that describes the state dynamics is

$$\dot{r} = -w \tag{16}$$

$$\dot{\phi} = \frac{u}{r} \tag{17}$$

$$\dot{\theta} = \frac{v}{r\cos\phi} - \Omega \tag{18}$$

$$\begin{Bmatrix} \dot{u} \\ \dot{v} \\ \dot{w} \end{Bmatrix} = \boldsymbol{R}_{\mathcal{CN}}^{\mathsf{T}} \begin{Bmatrix} a_x \\ a_y \\ a_z \end{Bmatrix} + \begin{Bmatrix} \left(uw - v^2\tan\phi\right)/r + g_u \\ \left(uv\tan\phi + vw\right)/r + g_v \\ -\left(u^2+v^2\right)/r + g_w \end{Bmatrix} \tag{19}$$

$$\begin{Bmatrix} \dot{e}_0 \\ \dot{e}_1 \\ \dot{e}_2 \\ \dot{e}_3 \end{Bmatrix} = \frac{1}{2}\begin{bmatrix} -e_1 & -e_2 & -e_3 \\ e_0 & -e_3 & e_2 \\ e_3 & e_0 & -e_1 \\ -e_2 & e_1 & e_0 \end{bmatrix} \left(\begin{Bmatrix} \omega_x \\ \omega_y \\ \omega_z \end{Bmatrix} - \frac{1}{r}\boldsymbol{R}_{\mathcal{CN}} \begin{Bmatrix} v \\ -u \\ -v\tan\phi \end{Bmatrix} \right) \tag{20}$$

where a_x, a_y, a_z, ω_x, ω_y and ω_z are the body-axis linear acceleration and angular rate measurements from the IMU. The matrix $\boldsymbol{R}_{\mathcal{CN}}$ is given by $\boldsymbol{R}_{\mathcal{CN}} = \boldsymbol{R}_{\mathcal{DN}}\boldsymbol{R}_{\mathcal{CD}}$, where

$$\boldsymbol{R}_{\mathcal{DN}} = \begin{bmatrix} e_0^2+e_1^2-e_2^2-e_3^2 & 2\left(e_1e_2+e_0e_3\right) & 2\left(e_1e_3-e_0e_2\right) \\ 2\left(e_1e_2-e_0e_3\right) & e_0^2-e_1^2+e_2^2-e_3^2 & 2\left(e_0e_1+e_2e_3\right) \\ 2\left(e_1e_3+e_0e_2\right) & 2\left(e_2e_3-e_0e_1\right) & e_0^2-e_1^2-e_2^2+e_3^2 \end{bmatrix} \tag{21}$$

$$\boldsymbol{R}_{\mathcal{CD}} = \begin{bmatrix} \cos(\phi_{td} - \phi) & 0 & \sin(\phi_{td} - \phi) \\ 0 & 1 & 0 \\ -\sin(\phi_{td} - \phi) & 0 & \cos(\phi_{td} - \phi) \end{bmatrix} \tag{22}$$

where ϕ_{td} is the topodetic latitude of the vehicle. The topodetic latitude and declination are related by the equation[34]

$$\tan\phi_{td} = \tan\phi + \frac{R_{\mathbb{Q}}\,\epsilon_{\mathbb{Q}}^2\,\sin\phi_{td}}{r\cos\phi\sqrt{1-\epsilon_{\mathbb{Q}}^2\,\sin^2\phi_{td}}} \tag{23}$$

The gravitational accelerations (g_u, g_v, and g_w) were computed using the truncated 25 degree and order GRGM660PRIM model developed from the GRAIL data described in the previous section.[29]

Filter Measurement Model The filter was configured to process each beam range and velocity measurement as an update step to correct the prediction based on numerical integration of the process model. An efficient ray-tracing algorithm originally developed for simulating Mars Science Laboratory radar measurements[35] was used to model the NDL beams. First, the NDL beams are assumed to be infinitely thin rays fixed to the vehicle structural frame with a specified origin and pointing direction. The ray-tracing algorithm then searches along the ray direction until an intersection with the terrain surface is detected. Once an intersection is determined, an interpolation scheme is used to compute the intersect coordinates and compute the along-beam range. This range is used within the Kalman filter as the measurement equation to compute residuals.

The ray-tracing algorithm is a component of a larger terrain modeling engine that integrates the DEM using efficient data loading methods. The raw DEM data, contained in a GeoTIFF file, is converted to a NetCDF file format,[36] which permits loading subsections of the DEM data such that memory management can be optimized by the user. Additionally, since the ray-tracing algorithm inherently assumes the underlying DEM data are represented in cylindrical coordinates, the polar-stereographic DEM data are converted to cylindrical coordinates prior to NetCDF conversion.[37]

The beam velocities are computed from the projection of the ground-relative velocity onto the beam pointing vector. The range and velocity measurement equations for Beam A are (equations for Beams B and C are of the same form)

$$\rho_A = \left\| \begin{Bmatrix} r\cos\phi\cos\theta - r_A\cos\phi_A\cos\theta_A \\ r\cos\phi\sin\theta - r_A\cos\phi_A\sin\theta_A \\ r\sin\phi - r_A\sin\phi_A \end{Bmatrix} + \boldsymbol{R}_{\mathcal{MN}}^{\mathsf{T}}\boldsymbol{r}_{NO} \right\| \tag{24}$$

$$\nu_A = \boldsymbol{s}_A \cdot \boldsymbol{R}_{\mathcal{SN}}^{\mathsf{T}} \left[\boldsymbol{R}_{\mathcal{CN}} \begin{Bmatrix} u \\ v \\ w \end{Bmatrix} + \boldsymbol{\omega} \times \boldsymbol{r}_{NO} - \boldsymbol{R}_{\mathcal{MN}} \begin{Bmatrix} -r_A\Omega\cos\phi_A\sin\theta_A \\ r_A\Omega\cos\phi_A\cos\theta_A \\ 0 \end{Bmatrix} \right] \tag{25}$$

where r_A, ϕ_A, and θ_A are the coordinates of the beam/surface intersection point computed from the ray-tracing algorithm. Note that these intersection points are functions of the vehicle position and attitude relative to the DEM. $\boldsymbol{R}_{\mathcal{MN}}$ is the matrix for the transformation from the lunar mean equator frame to the Nova-C body frame,[34]

$$\boldsymbol{R}_{\mathcal{MN}} = \begin{bmatrix} e_0^2+e_1^2-e_2^2-e_3^2 & 2(e_1e_2+e_0e_3) & 2(e_1e_3-e_0e_2) \\ 2(e_1e_2-e_0e_3) & e_0^2-e_1^2+e_2^2-e_3^2 & 2(e_0e_1+e_2e_3) \\ 2(e_1e_3+e_0e_2) & 2(e_2e_3-e_0e_1) & e_0^2-e_1^2-e_2^2+e_3^2 \end{bmatrix} \cdot \tag{26}$$

$$\begin{bmatrix} -\sin\phi_{td}\cos\theta & -\sin\phi_{td}\sin\theta & \cos\phi_{td} \\ -\sin\theta & \cos\theta & 0 \\ -\cos\phi_{td}\cos\theta & -\cos\phi_{td}\sin\theta & -\sin\phi_{td} \end{bmatrix} \tag{27}$$

The filter measurements consisting of beam ranges and velocities were assembled as

$$\boldsymbol{y} = \begin{bmatrix} \rho_A & \rho_B & \rho_C & \nu_A & \nu_B & \nu_C \end{bmatrix}^{\mathsf{T}} \tag{28}$$

The sensitivities of the measurement equation for the filter update step were computed using numerical partial derivatives.

TRAJECTORY RECONSTRUCTION RESULTS

This section describes the results of the NewSTEP trajectory reconstruction based on the NDL and IMU data. The Copernicus post-mission trajectory was used to obtain the initial conditions for the 6-DOF NewSTEP Kalman filter trajectory reconstruction process.

Some results of the trajectory reconstruction are shown in Figure 8. Figure 8(a) shows the altitude above ground level. This altitude was computed from the reconstructed position above the terrain height from the DEM. The altitude above ground level at the start of the NDL reconstruction where all three beams intersect with the surface of the Moon was 8017.7 m. The altitude above ground level at the start of the IMU data segment was 1934.3 m. The maximum difference between the two reconstructed altitudes was 83.1 m, which occurred close to the start of the IMU/NDL reconstruction. The two reconstructions agree to within approximately 5.6 m over the final minute of the trajectory. Note that the blue and black dashed curves correspond to the altitude above ground level. The NDL-only estimate is computed from the plane formed by the three range vector measurements and the curve corresponding to the IMU/NDL reconstruction is the altitude computed from the DEM. The red curve in Figure 8(a) is the IMU/NDL reconstructed altitude above the point of the vehicle's first touchdown on the lunar surface. The initial altitude above the landing site at the start of the IMU/NDL reconstruction was 1619.1 m. Differences between the altitude above ground level and the altitude above the landing site are due to local terrain variations that are captured in the DEM data. The 3σ uncertainties of the IMU/NDL altitude based on the Kalman filter state covariance are within 0.16 m over the time period, though note these uncertainties do not contain an estimate of the DEM altitude uncertainty.

Figure 8(b) shows the magnitude of the Moon-relative velocity. The initial velocity based on the NDL measurements was 543.3 m/s, and the final velocity at first contact with the ground was 7.79 m/s. The initial velocity based on the IMU/NDL reconstruction was 283.6 m/s and the velocity at the first ground contact was 7.82 m/s. The two reconstructions agree to within 0.36 m/s over the time period of the IMU/NDL reconstruction. The 3σ uncertainty of the IMU/NDL reconstruction is within 0.017 m/s.

The reconstructed vehicle pitch angles are shown in Figure 8(c). The NDL-only pitch angle is the attitude of the vehicle relative to the plane formed by the three range vector measurements. The IMU/NDL angle is computed relative to the surface normal given by the DEM. The two angles differ by up to 12.1 deg over the time period of the IMU/NDL reconstruction. The differences are mainly due to the apparent higher frequency content of the IMU/NDL reconstruction that results from the finer terrain resolution of the DEM compared to the coarse approximation based on the three range vector measurements. A third angle corresponding to the pitch relative to the local North-East-Down (NED) frame is shown with the red curve in Figure 8(c). This angle represents the attitude of the vehicle relative to the line tangent to the lunar reference ellipse rather than the local terrain. The differences between the two IMU/NDL angles are solely due to the terrain variation. The oscillations apparent in the ground-relative pitch angle are due to the local terrain rather than any attitude motion of the vehicle, as indicated by the smooth and slowly varying NED-relative curve. The reconstructed pitch attitude relative to the local terrain according to the DEM at the instant of first contact with the ground was 77.05 deg, and the corresponding pitch angle relative to NED was 85.43 deg. The reconstructed pitch angle 3σ uncertainties from the IMU/NDL reconstruction are within 0.18 deg.

The reconstructed flight path angle is shown in Figure 8(d). These data include the NDL-only terrain relative pitch angle and a similar angle computed based on the surface normal derived from the DEM. The maximum difference between the two reconstructed angles is 12.3 deg. Similar to the pitch angle, these differences are largely due to apparent high frequency signal that is caused by the terrain data captured in the DEM compared with the coarse slope estimate computed from

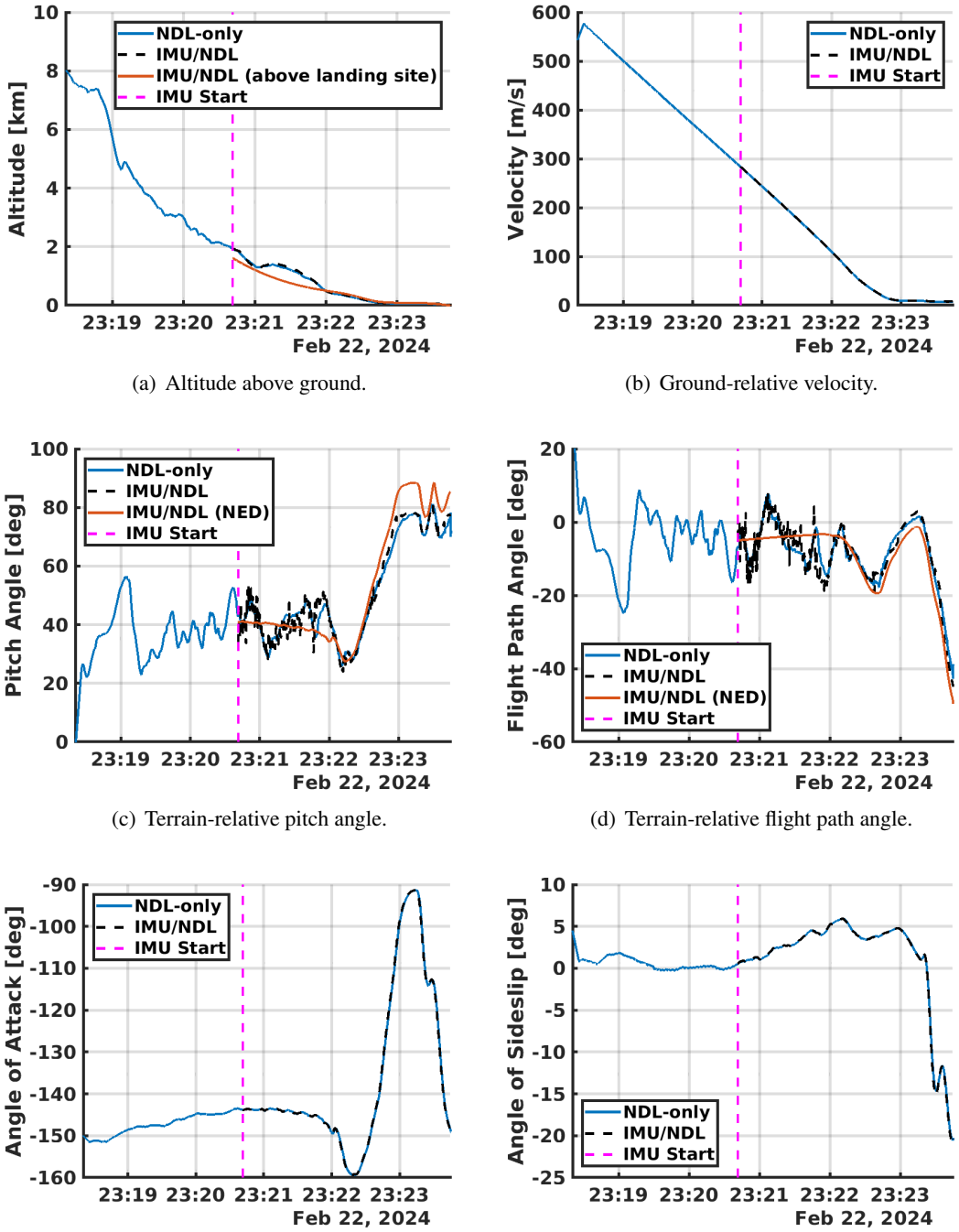

(a) Altitude above ground.

(b) Ground-relative velocity.

(c) Terrain-relative pitch angle.

(d) Terrain-relative flight path angle.

(e) Angle of attack.

(f) Sideslip angle.

Figure 8. Reconstructed trajectory.

the three range vector measurements. The red curve in Figure 8(d) corresponds to the flight path angle computed relative to the tangent of the local reference ellipse. The differences between the two IMU/NDL angles is again solely due to the terrain variations, and a similar conclusion as in the pitch angle can be reached, indicating that the oscillations in the ground-relative angle are due to variations in the terrain and not tied to motion of the vehicle, given the smooth variation in the NED-relative angle. The ground-relative and NED relative flight path angles at the moment of first contact with the ground were -44.39 and -49.07 deg, respectively. The 3σ uncertainties in the IMU/NDL reconstructed flight path angle were within 0.025 deg.

The reconstructed angles of attack and sideslip are shown in Figure 8(e) and (f), respectively. These angles represent the attitude of the vehicle with respect to the Moon-relative velocity vector. Differences between the angles computed directly from the NDL measurements and the IMU/NDL reconstruction are within 0.43 deg in angle of attack and 0.54 deg in the sideslip angle. The 3σ uncertainties in each angle from the IMU/NDL reconstruction are within 0.025 deg.

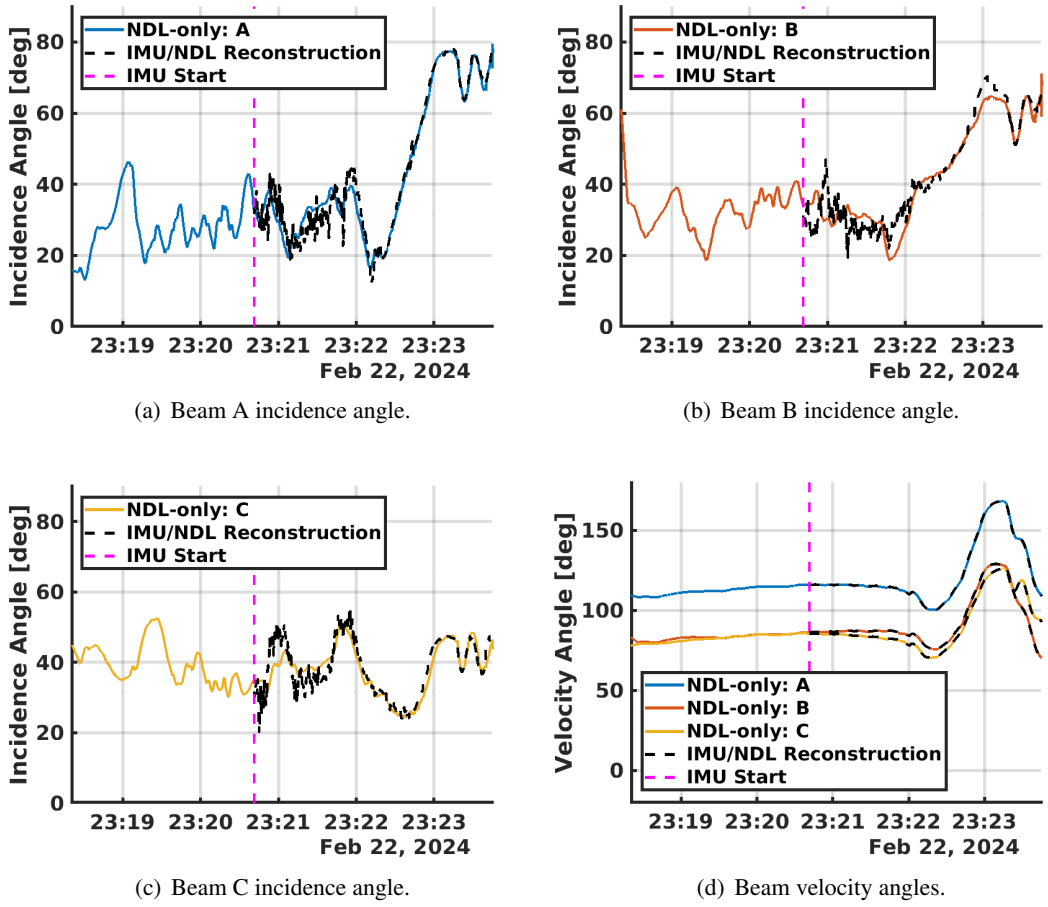

(a) Beam A incidence angle.

(b) Beam B incidence angle.

(c) Beam C incidence angle.

(d) Beam velocity angles.

Figure 9. Incidence and velocity angles.

The reconstructed incidence and velocity angles are shown in Figure 9. The NDL-only incidence angles are computed as the intercept angle between the beam and the plane formed by the three range vector measurements, whereas the IMU/NDL reconstructed angles are computed based on the angle between the beam and the surface normal from DEM. The differences across all three beam incidence angles are within 16.7 deg. As previously noted, the differences are largely due to the finer terrain resolution captured by the DEM compared to the coarse estimate based on the plane formed by the three range vector measurements. The velocity angle differences between the two reconstructions are within 0.31 deg across all three beam directions. Note that although Beams B and C have symmetric pointing directions, their velocities incidence angles do not exactly match during the IMU/NDL phase of the reconstruction. These differences arise to the ability of the 6-DOF trajectory reconstruction to estimate the vehicle roll attitude. The reconstructed roll attitude varies between -45 to +90 deg over the last 90 s of the flight.

The beam A residuals from the IMU/NDL reconstruction are shown in Figure 10. Note that the timescale here corresponds to the time range from the overlap between the IMU and NDL data. The residuals are computed as the difference between the NDL measurement and the corresponding filter prediction based on the reconstructed trajectory. The 3σ uncertainties are computed based

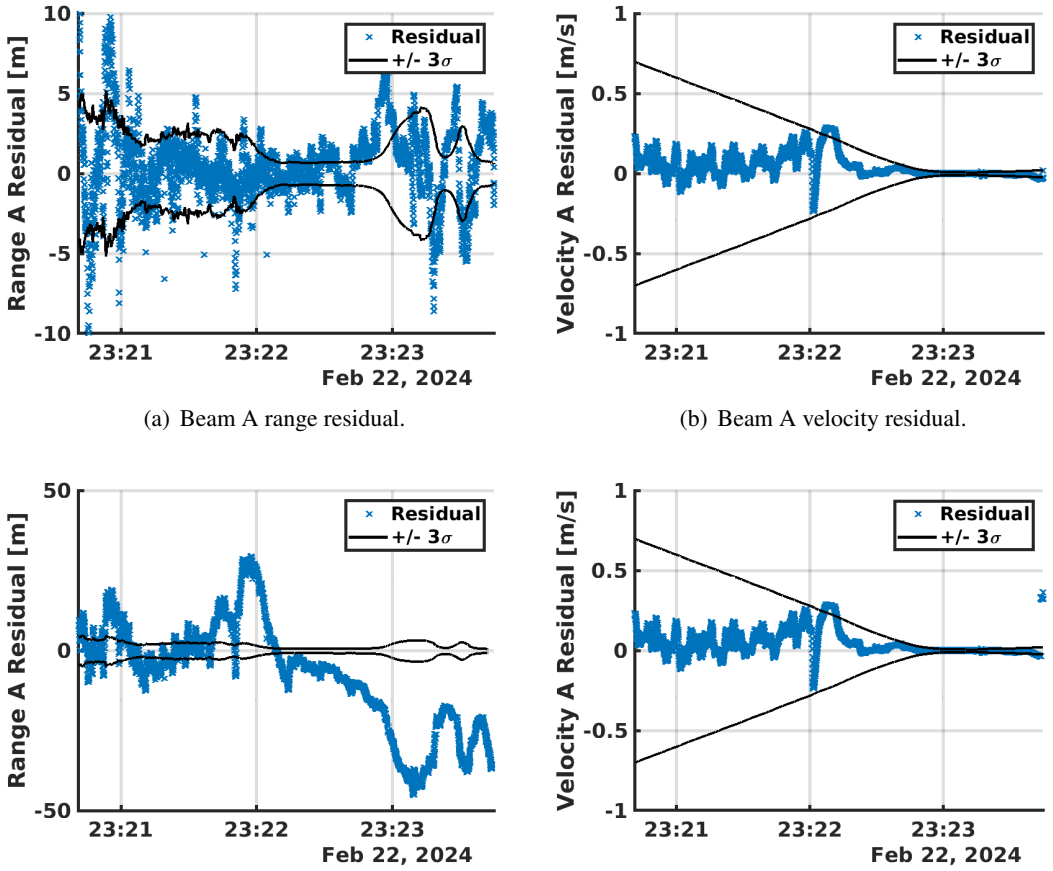

(a) Beam A range residual.

(b) Beam A velocity residual.

(c) Beam A range residual with coarse DEM.

(d) Beam A velocity residual with coarse DEM.

Figure 10. NDL Beam A measurement residuals.

on the combination of measurement uncertainty and the state error covariance projected into the measurement space. The range and velocity residuals in Figures 10(a) and (b), respectively, are approximately centered on a value of zero and the values are largely encapsulated by the 3σ uncertainty bounds. These results indicate that the reconstruction filter is consistent in the sense that the differences are bounded by the predicted uncertainties. Some excursions in the range residuals compared to the uncertainty bounds shown in Figure 10(a) could be due to the assumption of no uncertainties in the DEM terrain elevation model. The beam velocity residual uncertainties shown in Figure 10(b) are notably conservative early in the trajectory, and were found to be due to the beam alignment uncertainties. The beam measurement residuals for channels B and C produce similar results and are therefore not shown here.

The sensitivities of the beam residuals with respect to the DEM resolution are illustrated in Figures 10(c) and (d). Here a coarser DEM with 120 m per pixel resolution was used to evaluate the range and velocity measurements along the reconstructed trajectory. The magnitude of the range residuals from the 120 m DEM shown in Figure 10(c) are clearly larger that corresponding to the finer 30 and 20 m DEM resolution shown in Figure 10(a). The residuals based on the 120 m resolution DEM are not encapsulated by the predicted 3σ bounds computed from the filter covariance. Note that no adjustment to account for DEM terrain elevation uncertainty was included in these calculations. The velocity residual from the coarse 120 m DEM shown in Figure 10(d) is less sensitive to the DEM resolution that the position residuals. This result is due to the Doppler-based beam velocity measurements rather than a range-rate type measurement that would be more sensitive to the terrain model.

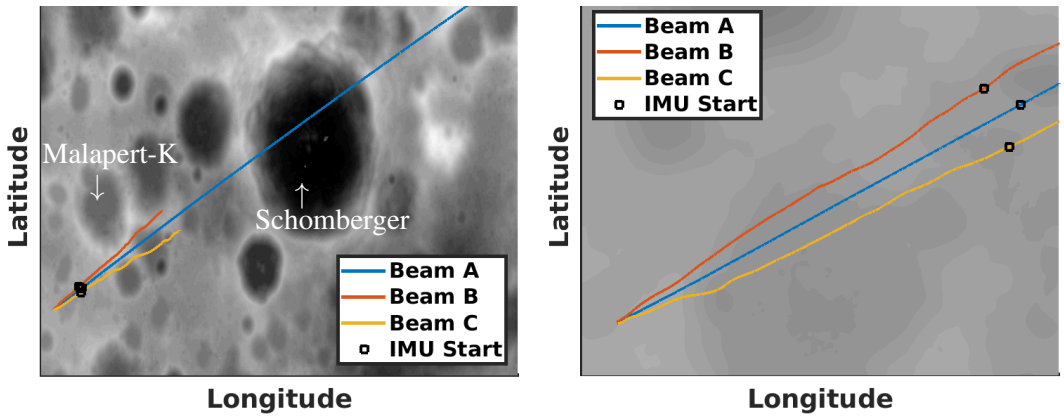

(a) Beam/surface intersection.

(b) Beam/surface intersection (detail during portion of trajectory where IMU data are available).

Figure 11. NDL beam/surface intersection ground tracks.

The suspected terrain features in the range measurement data were investigated by extracting the latitude and longitude of the beam/surface intersection point and comparing that to a map of the lunar surface. The crater crossings can be visualized by plotting the ground track of the beam/surface intersections along the DEM terrain model. The NDL beam/surface intersection ground tracks are shown in Figure 11. Recall that Beam A points approximately in the vehicle nadir direction. Beam A crossed through Shomberger crater early in the trajectory, as evident in the feature shown in Figure 6(a) that peaks at approximately 23:16 UTC. Beam C crosses over four unnamed craters to the south of crater Malapert K during the vehicle's approach to the landing site. These crossings can be noted by features in the Beam C range data shown in Figure 6(a) at 23:18:40, 23:19:20, 23:19:57, and 23:21:47, respectively. For purposes of scale, note that Shomberger and Malapert K craters have diameters of approximately 85 km and 46 km, respectively. The traversed ground tracks from the first data point to the moment of touchdown are approximately 345 km for Beam A, 79 km for Beam B, and 85 km for Beam C.

A detailed view of the beam/surface intersection ground tracks over the time period where IMU data was available is shown in Figure 11(b). This figure shows the crossing of Beam C through the fourth crater described previously, which lies to the south of the vehicle groundtrack and to the east of the landing site. The high level of agreement between the observed and simulated beam range measurements, coupled with tying the observed range changes to the DEM using the ground tracks, is additional validation of the terrain engine.

TRAJECTORY ANIMATION

The reconstructed trajectory was input to the Exploration Visualization Environment (EVE).[38] EVE is a tool that can create engineering animations and visualizations based on trajectory data and a graphics geometry of the vehicle. EVE is capable of calculating several kinds of quantities of interest along a given trajectory. For this problem, EVE was configured to compute the beam ranges based on the trajectory data and EVE's independent implementation of the lunar DEM. These outputs provide an independent check of the DEM implementation by comparing the reconstructed ranges to the EVE-computed ranges.

An example image from the animation is shown in Figure 12. Two simultaneous views of the trajectory are shown in Figure 12. A close-in view of the lander is shown in the left panel and a larger scale view is shown to the right. In both cases, the three NDL beams are shown emanating from the sensor. The right panel shows the three beams impinging on the lunar surface. Note that Beam C is crossing through a crater at this instant in time. The vehicle trajectory line is also shown in the image.

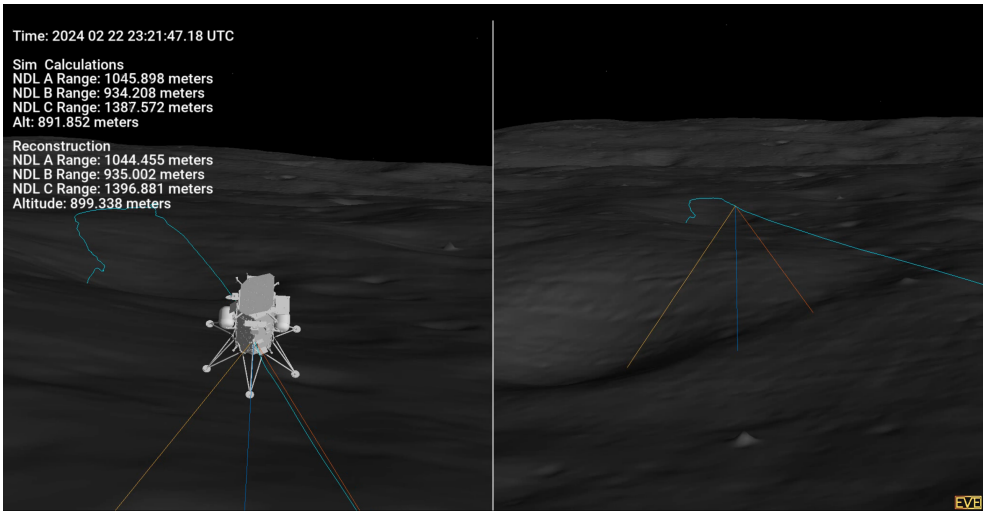

Figure 12. EVE animation still image during Beam C crater impingement.

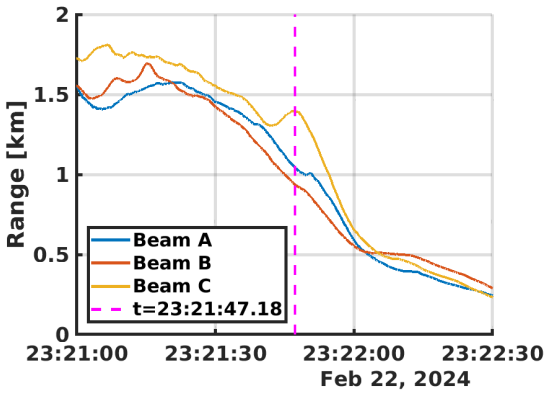

Figure 13. Beam ranges during crater crossing.

The calculated and reconstructed NDL beam ranges are shown in the upper left. The ranges labeled as *Sim Calculations* are those computed from EVE's internal model of the lunar surface, the reconstructed trajectory, and the NDL beam pointing directions. Those labeled as *Reconstruction* are computed from NDL pointing directions, the reconstructed trajectory, and the NewSTEP lunar DEM implementation that was used internally for processing the beam range measurements in the Kalman filter. The two range calculations are computed from same trajectory and NDL beam geometry but each use an independent implementation of the lunar terrain model. The independent range calculations match to within several meters, which serves as a verification of the terrain model implementation used in the reconstruction.

CONCLUSION

The Navigation Doppler Lidar sensor was flown on the Intuitive Machines IM-1 Odysseus Lunar lander on its mission to the Moon in February 2024. The sensor acquired range and velocity data during the descent and landing on the lunar surface that exceeded preflight expectations. These data were combined with linear accelerations and angular rates from an inertial measurement unit in an extended Kalman filter to reconstruct the final three minutes of the landing trajectory to the point of first contact with the surface. The filter utilized a ray tracing terrain engine that integrated a digital elevation model of the Lunar surface. Terrain features such as craters were observed in the data and confirmed by comparison with digital elevation maps of the lunar surface. This reconstruction effort

showed that the modeled lidar beam ranges and velocities derived from the reconstructed trajectory agreed to within approximately 5 m and 0.5 m/s of the measurements, respectively, indicating high measurement accuracy and flight validation of the terrain engine and underlying elevation data.

ACKNOWLEDGMENTS

This work was funded under the Technology Engineering and Aerospace Mission Support 3 (TEAMS3) contract number 80LARC17C0003 with NASA Langley Research Center. The NDL sensor development was supported by multiple NASA program offices including the Space Technology Mission Directorate, Science Mission Directorate's Exploration Program Office, Commercial Lunar Payload Services, and Langley Research Centers's Director's Office, Space Technology and Exploration Directorate, and Engineering Directorate. The authors gratefully acknowledge helpful discussion provided by Shaun Stewart, Andrew Hollister, and Giovanni Molina-Ramos of Intuitive Machines. Additional visualization support for this paper was provided by Michael S. Manwell and assistance in creating the surface terrain plot in Figure 11 was provided by James W. Williams, both with Analytical Mechanics Associates.

NOTATION

a_x, a_y, a_z	Body axis sensed linear accelerations, m/s^2
e_0, e_1, e_2, e_3	Euler parameters for the transformation from topodetic frame to body frame
g_u, g_v, g_w	Topocentric gravity components, m/s^2
h_p	Height above plane formed by NDL measurements, m
$\boldsymbol{n}$	Surface normal unit vector
$\boldsymbol{R}_{\mathcal{CN}}$	Rotation matrix from local topocentric frame to Nova-C vehicle frame
$\boldsymbol{R}_{\mathcal{CD}}$	Rotation matrix from local topocentric frame to topodetic frame
$\boldsymbol{R}_{\mathcal{DN}}$	Rotation matrix from local topodetic frame to Nova-C vehicle frame
$\boldsymbol{R}_{\mathcal{MN}}$	Rotation matrix from Moon Mean Equator frame to Nova-C vehicle frame
$\boldsymbol{R}_{\mathcal{SN}}$	Rotation matrix from NDL sensor frame to Nova-C vehicle frame
$R_{\leftmoon}$	Lunar mean equatorial radius, m
$\boldsymbol{r}_{AB}$, $\boldsymbol{r}_{AC}$, $\boldsymbol{r}_{BC}$	Position vector from point A to point B, A to C, and B to C, m
$\boldsymbol{r}_{OA}$, $\boldsymbol{r}_{OB}$, $\boldsymbol{r}_{OC}$	Position vector from point O to point A, B, and C, m
$\boldsymbol{r}_{NO}$	Position of the NDL sensor frame origin from the Nova-C body frame origin, m
r	Radius of the vehicle center of mass measured from the center of the Moon, m
$\boldsymbol{S}$	NDL sensor pointing matrix
$\boldsymbol{s}_A$, $\boldsymbol{s}_B$, $\boldsymbol{s}_C$	Beam A, B, and C pointing vectors in the NDL sensor frame
u	X (North) component of topocentric inertial velocity, m/s
$\boldsymbol{V}$	Ground-relative velocity in the body frame, m/s
V_x, V_y, V_z	Body frame components of the ground-relative velocity, m/s
v	Y (East) component of topocentric inertial velocity, m/s
w	Z (-Radial) component of topocentric inertial velocity, m/s
$\boldsymbol{x}$	Filter state
$\boldsymbol{y}$	Filter measurement
α	Angle of attack, rad
α_T	Total angle of attack, rad
β	Angle of sideslip, rad
γ	Ground-relative flight path angle, rad
$\epsilon_{\leftmoon}$	Eccentricity of lunar reference ellipse
ζ	Ground-relative pitch angle, rad
η_A, η_B, η_C	Beam A, B, and C velocity angles, rad
θ	Longitude angle, rad
λ_A, λ_B, λ_C	Beam A, B, and C incidence angles, rad

ν_A, ν_B, ν_C	Beam A, B, and C velocity measurements, m/s
ρ_A, ρ_B, ρ_C	Beam A, B, and C range measurements, m
σ	Standard deviation
ϕ	Declination angle, rad
ϕ_{td}	Topodetic latitude angle, rad
Ω	Angular velocity of the moon, rad/s
$\boldsymbol{\omega}$	Body axis angular velocity, rad/s
$\omega_x, \omega_y, \omega_z$	Body axis angular velocity components, rad/s

REFERENCES

[1] Amzajerdian, F., Petway, L., Hines, G., Barnes, B., Pierrottet, D., and Lockard, G., "Doppler Lidar Sensor for Precision Landing on the Moon and Mars," IEEE Aerospace Conference, March 2012. doi: 10.1109/AERO.2012.6187004

[2] Eichler, J., "A Performance Study of he Lunar Module's Landing Radar System," *Journal of Spacecraft and Rockets*, Vol. 5, No. 9, 1968, pp. 1016-1022. doi: 10.2514/3.29414

[3] Belz, J. E., Chen, C., and Cichy, B., "Phoenix Landing Radar Heatshield Anomaly," *Journal of Spacecraft and Rockets*, Vol. 48, No. 5, 2011, pp. 772-777. doi: 10.2514/1.51801

[4] Chen, C. W. and Pollard, B. D., "Radar Terminal Descent Sensor Performance During Mars Science Laboratory Landing," *Journal of Spacecraft and Rockets*, Vol. 51, No. 4, 2014, pp. 1208-1216. doi: 10.2514/1.A32641

[5] Epp, C. D., Robertson, E. A., and Brady, T., "Autonomous Landing and Hazard Avoidance Technology (ALHAT)," IEEE Aerospace Conference, March 2008. doi: 10.1109/AERO.2008.4526297

[6] Pierrottet, D., Amzajerdian F., Larry Petway, L., Barnes, B., and Lockard, G., "Flight Test Performance of a High Precision Navigation Doppler Lidar," Proc. SPIE 7323, Laser Radar Technology and Applications XIV, 732311, May 2009. doi: 10.1117/12.821902

[7] Pierrottet, D., Amzajerdian, F., Petway, L., Barnes, B., Lockard, G., and Hines, G., "Navigation Doppler Lidar Sensor for Precision Altitude and Vector Velocity Measurements: Flight Test Results," Proc. SPIE 8044, Sensors and Systems for Space Applications IV, 80440S, May 2011. doi: 10.1117/12.886826

[8] Pierrottet, D. F., Amzajerdian, F., Petway, L., Hines, G., and Barnes, B., "Field Demonstration of a Precision Navigation Lidar System for Space Vehicles," AIAA Paper 2013-4717, August 2013. doi: 10.2514/6.2013-4717

[9] Carson III, J. M., Robertson, E. A., Trawny, N., Amzajerdian, F., "Flight Testing ALHAT Precision Landing Technologies Integrated Onboard the Morpheus Rocket Vehicle," AIAA Paper 2015-4417, August 2015. doi: 10.2514/6.2015-4417

[10] Amzajerdian, F., Hines, G. D., Petway, L. B., Barnes, B. W., Pierrottet, D. F., and Carson, J. M., "Development of Navigation Doppler Lidar for Future Landing Mission," AIAA Paper 2016-5590, September 2016. doi: 10.2514/6.2016-5590

[11] Amzajerdian, F., Hines, G. D., Pierrottet, D. F., Barnes, B. W., Petway, L. B., and Carson, J. M., "Demonstration of Coherent Doppler Lidar for Navigation in GPS-Denied Environments," Proc. SPIE 10191, Laser Radar Technology and Applications XXII, 1019102, May 2017. doi: 10.1117/12.2266972

[12] Restrepo, C. I., Carson III, J. M., Amzajerdian, F., Seubert, C. R., Lovelace, R. S., McCarthy, M. M., Tse, T., Stelling, R., and Collins, S. M., "Open-Loop Performance of COBALT Precision Landing Payload on a Commercial Sub-Orbital Rocket," AIAA Paper 2018-0613, January 2018. doi: 10.2514/6.2018-0613

[13] Pierrottet, D. F., Hines, G. D., Barnes, B. W., Amzajerdian, F., Petway, L. B., and Carson III, J. M., "Navigation Doppler Lidar Integrated Testing Aboard Autonomous Rocket Powered Vehicles," AIAA Paper 2018-0614, January 2018. doi: 10.2514/6.2018-0614

[14] Sostaric, R. R., Carson III, J. M., Pedrotty, S. M., Rutishauser, D. K., Tse, T., Sooknanan, J. W., Amzajerdian, F., Dwyer Cianciolo, A., Kuhl, C. A., Blair, J. B., Chen G. T., and Chen, P-T., "The SPLICE Project: Safe and Precise Landing Technology Development and Testing," AIAA Paper 2021-0256, January 2021. doi: 10.2514/6.2021-0256

[15] Gragossian, A., Pierrottet, D., Estes, J., Barnes, B. W., Amzajerdian, F., and Hines, G., D., "Navigation Doppler Lidar Performance at High Speed and Long Range," AIAA Paper 2020-0369, January 2020. doi: 10.2514/6.2020-0369

[16] Bieniawski, S., Lewis, B., Friia, B., Mahajan, A., Somervill, K., Mamidipudi, P., and Daykin, D., "New Shepard Flight Test Results from Blue Origin De-Orbit Descent and Landing Tipping Point," AIAA Paper 2022-1829, January 2022. doi: 10.2514/6.2022-1829

[17] Bieniawski, S., Polaha, J., Friia, B., and Forrest, M., "De-orbit Descent and Landing Tipping Point Program Final Report," NASA Contract Number 80LARC19C0005, January 17th, 2022. https://ntrs.nasa.gov/citations/20210026314

[18] Williams, J., Woffinden, D., and Putnam, Z. R., "Mars Entry Guidance and Navigation Analysis Using Linear Covariance Techniques for the Safe and Precise Landing – Integrated Capabilities Evolution (SPLICE) Project," AIAA Pape 2020-0597, January 2020. doi: 10.2514/6.2020-0597

[19] Lugo, R. A., Cianciolo, A. D., Williams, R. A., Dutta, S., Powell, R. W., and Chen, P-T., "Integrated Precision Landing Performance and Technology Assessments of a Human-Scale Mars Lander Using a Generalized Simulation Framework," AIAA Paper 2022-0607, January 2022. doi: 10.2514/6.2022-0607

[20] Lugo, R. A., Cianciolo, A., Dutta, S., Williams, R. A., Green, J. S., Chen, P-T., D'Souza, S., and Pensado, A. R., "Precision Landing Performance of a Human-Scale Lunar Lander Using a Generalized Simulation Framework," AIAA Paper 2022-0609, January 2022. doi: 10.2514/6.2022-0609

[21] Hines, G., Amzajerdian, F., Gragossian, A., Karlgaard, C., Angster, S., Lugo, R., and Litton, D., "Demonstration of Navigation Doppler Lidar Capabilities Onboard the First Commercial Lunar Lander," AIAA Paper 2025-1115, January 2025. doi: 10.2514/6.2025-1115

[22] Kuettel, D. H., Leonard, J. M., Geeraert, J. L., Sallnas, M. J., Ge, S., Welsh, S., Antreasian, P. G., and Stewart, S., "IM-1 Orbit Determination: A Comparison of Mission Deliveries vs. Post-Flight Trajectory Reconstruction," AAS Paper 24-282, August 2024.

[23] Stewart, S., Johnson, W., Busic, C. J., Leonard, J., Geeraert, J. L., and Salinas, M. J., "Maneuver Execution Performance for the IM-1 Nova-C Lunar Mission," AAS Paper 25-155, January 2025.

[24] Stewart, S., Johnson, W., Hollister, A., Leonard, J., and Matthews, B., "IM-1 Powered Descent Reconstruction," AAS Paper 25-310, January 2025.

[25] Moon, Q. and Geller, D. K., "Batch Dilution of Precision Optimal Navigation Planning for Cislunar Environments," *The Journal of the Astronautical Sciences*, Vol. 70, No. 44, 2023, pp. 1-22. doi: 10.1007/s40295-023-00409-4

[26] Karlgaard, C., Tartabini, P., Blanchard, R., Kirsch, M., and Toniolo, M., "Hyper-X Post-Flight Trajectory Reconstruction," *Journal of Spacecraft and Rockets*, Vol. 43, No. 1, 2006, pp. 105-115. doi: 10.2514/1.12733

[27] Amzajerdian, F., Gragossian, A., Hines, G. D., Barnes, B. W., Cisewski, M. S., and Pierrottet, D. F., "Analysis of Navigation Doppler Lidar Performance for Moon and Mars landing," AIAA Paper 2022-1712, January 2022. doi: 10.2514/6.2022-1712

[28] Barker, M. K., Mazarico, E., Neumann, G. A., Smith, D. E., Zuber, M. T., Head, J. W., and Sun, X., "A New View of the Lunar South Pole from the Lunar Orbiter Laser Altimeter (LOLA)," *The Planetary Science Journal*, Vol. 4, No. 183, September 2023. doi: 10.3847/PSJ/acf3e1

[29] Lemoine, F. G., Goossens, S., Sabaka, T. J., Nicholas, J. B., Mazarico, E., Rowlands, D. D., Loomis, B. D., Chinn, D. S., Caprette, D. S., Neumann, G. A., Smith, D. E., and Zuber, M. T., "High-Degree Gravity Models from GRAIL Primary Mission Data," *Journal of Geophysical Research: Planets*, Vol. 118, 2013, pp. 1676-1699. doi: 10.1002/jgre.20118

[30] Moore, J. W., Roorda, T., Greer, D., and Stewart, S., "Maneuver Planning and Analysis with Copernicus for the IM-1 Mission," AAS Paper 24-350, August 2024.

[31] Karlgaard, C., Beck, R., Derry, S., Brandon, J., Starr, B., Tartabini, P., and Olds, A., "Ares I-X Trajectory Reconstruction: Methodology and Results," *Journal of Spacecraft and Rockets*, Vol. 50, No. 3, 2013, pp. 641-661. doi: 10.2514/1.A32345

[32] Karlgaard, C., Kutty, P., Schoenenberger, M., Munk, M., Little, A., Kuhl, C., and Shidner, J., "Mars Science Laboratory Entry Atmospheric Data System Trajectory and Atmosphere Reconstruction," *Journal of Spacecraft and Rockets*, Vol. 51, No. 4, 2014, pp. 1029-1047. doi: 10.2514/1.A32770

[33] Karlgaard, C. D., Schoenenberger, M., Dutta, S., and Way, D. W., "Mars Entry, Descent, and Landing Instrumentation 2 Trajectory, Aerodynamics, and Atmosphere Reconstruction," *Journal of Spacecraft and Rockets*, Vol. 60, No. 1, 2023, pp. 199–214. doi: 10.2514/1.A35440

[34] Vallado, D. A., *Fundamentals of Astrodynamics and Applications*, McGraw-Hill, New York, 1997, pp. 20-50, 202-204.

[35] Shidner, J., "An Efficient Ray-Tracing Method for Determining Terrain Intercepts in EDL Simulations," IEEE Aerospace Conference, Big Sky, MT, March 2016. doi: 10.1109/AERO.2016.7500591

[36] NSF Unidata, "Network Common Data Form (NetCDF)," UCAR/NSF Unidata Program Center, Boulder, CO. doi: 10.5065/D6H70CW6

[37] Lugo, R., Shidner, J., Williams, R. A., and Dutta, S., "Efficient and Accurate Terrain Integration & Application to Modeling & Simulation of Planetary Landing Systems," 21st International Planetary Probe Workshop, June 8th-14th, 2024, Williamsburg, VA, USA.

[38] Salas, A., Merrill, R., Angster, S., Caldwell, D., Hoffman, J., White, A., and Biron, P., "Exploration Visualization Environment," NASA Tech Briefs, Vol. 40, No. 3, March 2016.